

Using carrier-depletion silicon modulators for optical power monitoring

Hui Yu,^{1,*} Dietmar Korn,² Marianna Pantouvaki,³ Joris Van Campenhout,³ Katarzyna Komorowska,²
Peter Verheyen,³ Guy Lepage,³ Philippe Absil,³ David Hillerkuss,² Luca Alloatti,²
Juerg Leuthold,² Roel Baets,¹ and Wim Bogaerts¹

¹Photonics Research Group, Department of Information Technology, Ghent University-imec, Center for Nano- and Biophotonics (NB Photonics), St.-Pietersnieuwstraat 41, Gent 9000, Belgium

²Institute of Photonics and Quantum Electronics (IPQ) and Institute of Microstructure Technology (IMT), Karlsruhe Institute of Technology (KIT), Karlsruhe 76131, Germany

³imec, Kapeldreef 75, Leuven 3001, Belgium

*Corresponding author: hyu@intec.ugent.be

Received September 5, 2012; accepted September 25, 2012;
posted October 12, 2012 (Doc. ID 175667); published November 9, 2012

Defect-mediated subbandgap absorption is observed in ion-implanted silicon-on-oxide waveguides that experience a rapid thermal annealing at 1075°C. With this effect, general carrier-depletion silicon modulators exhibit the capability of optical power monitoring. Responsivity is measured to be 22 mA/W for a 3 mm long Mach-Zehnder modulator of $2 \times 10^{18} \text{ cm}^{-3}$ doping concentration at -7.1 V bias voltage and 5.9 mA/W for a ring modulator of $1 \times 10^{18} \text{ cm}^{-3}$ doping concentration at -10 V bias voltage. The former is used to demonstrate data detection of up to 35 Gbits/s. © 2012 Optical Society of America

OCIS codes: 250.7360, 230.7020, 250.0040.

An objective of silicon photonics is to integrate different functionalities, including wavelength multiplexing and demultiplexing, routing, optical emission, modulation, and detection on the silicon-on-oxide (SOI) platform by leveraging the advanced complementary metal-oxide semiconductor (CMOS) process technology. In case of power monitoring and detection, the 1.12 eV indirect bandgap of defect-free bulk silicon makes it transparent in telecom wavelength bands around 1.31 and 1.55 μm . In addition to the incorporation of germanium or III-V semiconductors into a silicon photonic circuit by epitaxial growth or bonding techniques [1], there are two intrinsic subbandgap absorption mechanisms that can give rise to a photocurrent inside an SOI waveguide: surface-state absorption (SSA) [2] and two-photon absorption (TPA) [3]. In order to enhance SSA and TPA, the cross section of an SOI waveguide was tailored to enlarge the overlap of the optical mode with the waveguide surface [4]; also, high-Q photonic crystal cavities were employed to achieve a high optical intensity at a reasonable input power [5,6]. Another mechanism that can generate a photocurrent from IR light in silicon is the defect-mediated subbandgap absorption. Crystal defects and associated midbandgap states that facilitate the IR optical absorption were induced by selectively implanting Si^+ [7–10], B^+ [11], He^+ [12], or protons [13] with proper doses and energies.

Generally, the photoactive crystal defects include divacancies and interstitial clusters. Divacancies are annealed out of the silicon between 150°C and 300°C, while interstitial clusters are believed to remain stable up to 600°C [9,10]. Doylend *et al.* reported that the photocurrent due to defect-mediated absorption decreases by a factor of 100 as the annealing temperature rises from 150°C to 400°C [14]. The highest annealing temperature among these defect dependent devices is 475°C [9,10]. It is not clear whether the effect can be observed after annealing at higher temperatures. In this Letter we use the

defect-state mediated absorption for an integrated power-monitoring function to avoid increasing the fabrication complexity. While the observed effect is generally much weaker than the direct absorption in a Ge or III-V photodiode, the functionality can be implemented relying exclusively on silicon carrier-depletion modulators without adding processing steps.

The carrier-depletion modulator is becoming a preferred solution for electro-optic modulation in silicon as a result of its CMOS compatibility, processing simplicity, and high operation speed. With this structure, PN junctions are embedded in SOI waveguides by ion implantation. After that, a rapid thermal annealing (RTA) above 1000°C activates the dopants and repairs damage in the silicon lattice without causing much dopant redistribution. Still, there remain some residual crystal defects that can mediate subbandgap absorption. After being heated to 1075°C, a reversed-biased silicon waveguide diode still produces a substantial photocurrent. This means that we can obtain from the carrier-depletion modulator an additional functionality as a power monitor.

The modulator used to characterize the photocurrent is a ring resonator with a lateral PN junction as shown in Fig. 1. Fiber grating couplers are used to couple the light in and out. The ring radius and the gap between the ring and the bus waveguide are 40 μm and 570 nm, respectively. The rib waveguide has a width of 450 nm, a height of 220 nm, and an etch depth of 70 nm. The nominal

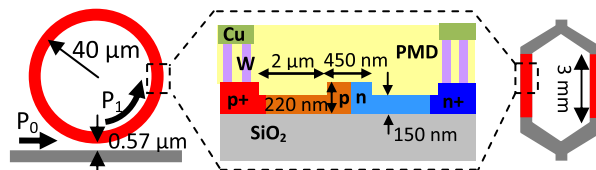


Fig. 1. (Color online) Schematic diagram of lateral PN-junction-based ring and Mach-Zehnder modulators. PMD, pre-metal dielectric.

doping concentration of the PN junction is $1 \times 10^{18}/\text{cm}^3$, while the contact regions beside the waveguide are heavily doped to $1 \times 10^{20}/\text{cm}^3$ to ensure ohmic contacts. The device was initially designed and then fabricated by the 200 mm line of imec for 10 Gbit/s modulation with a driving voltage of $<1 V_{pp}$ [15]. An elaboration of the processing flow can be found in our previous work [16]. We note that the highest temperature in the whole processing flow was 1075°C during the RTA. Unlike the previous works, which all require dedicated ion implantation and annealing to introduce defects [7–13], we take advantage of residual defects after RTA, and thus no additional processing steps are needed. This also means no additional absorption (and therefore optical loss) mechanism is introduced into the modulator.

Discrete points in Fig. 2(a) show measured transmission spectra of the device at different reverse bias points when the laser power is 0.5 mW. Since the power coupled out from the device at off-resonance wavelengths is 0.02 mW (-16.9 dBm), we estimate that the on-chip power in the bus waveguide before entering the coupling section of the ring is $P_0 = 0.1$ mW by assuming that the input and the output grating couplers have the same coupling efficiency. We extract the resonance wavelength shift $\Delta\lambda$, cross-coupling coefficient K between the ring and the bus waveguide, and the beam propagation loss of the ring from the transmission spectra by curve fitting. The fitting results are shown as dashed curves in Fig. 2(a). The variation of $\Delta\lambda$ and the loss with the reverse bias are plotted in Fig. 2(b). With good approximation, the value of K is considered to be fixed at 0.33. The propagation loss of 14.6 dB/cm at 0 V is quite reasonable for the utilized doping level. The defect-mediated absorption should be insignificant compared with the free carrier absorption. With the value of $\Delta\lambda$, K and the propagation loss, we calculate the power inside the ring after exiting the coupling section (P_1 as shown in Fig. 1). It is depicted in Fig. 2(c) as a function of the wavelength for different reverse biases.

The DC photocurrent as a function of wavelength was recorded simultaneously when we measured the spectra in Fig. 2(a). The result is shown in Fig. 3(a). Only photo-carriers in the carrier-depletion region are drifted by the electrical field and then contribute to the photocurrent

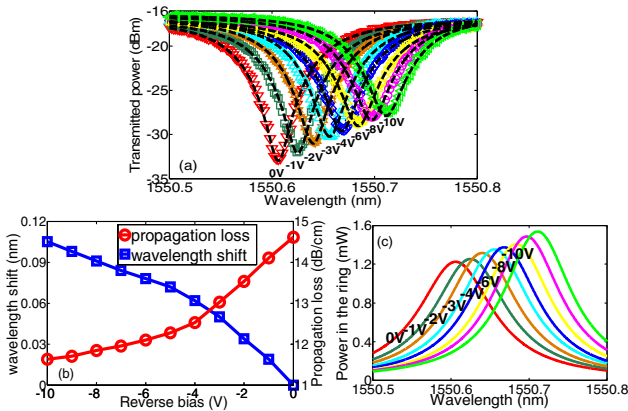


Fig. 2. (Color online) (a) Transmission spectra of the ring at different biases. (b) Resonance wavelength shift and propagation loss of the ring versus bias. (c) Power P_1 inside the ring for different biases.

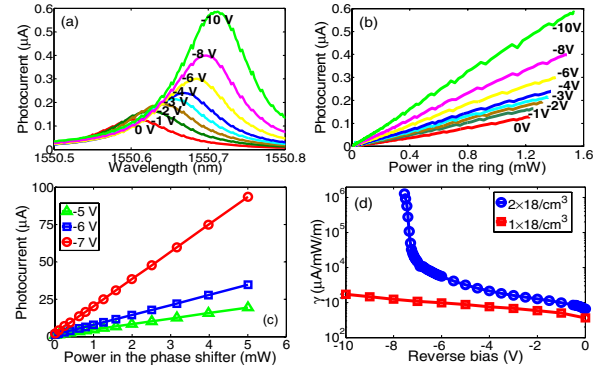


Fig. 3. (Color online) (a) Spectra of DC photocurrent at different biases. (b) Photocurrent versus optical power in the ring. (c) Photocurrent versus optical power in one phase shifter of the Mach-Zehnder modulator. (d) Carrier generation efficiency γ versus bias for two doping concentrations.

efficiently. Therefore, as the reverse bias increases in Fig. 3(a), the photocurrent is enhanced by the expanded carrier-depletion region. Combining Figs. 2(c) and 3(a), we map the relationship between the power P_1 in the ring and the photocurrent as shown in Fig. 3(b). Ripples in Figs. 3(a) and 3(b) result from the Fabry-Perot cavity effect between the two fiber grating couplers. It can be seen that a linear absorption mechanism rules the generation of photocurrent. As previously mentioned, there are two linear absorptions inside an SOI waveguide: defect-mediated absorption and SSA. Before we conclude that the current is caused by residual defects, it is necessary to estimate the contribution from SSA. Chen *et al.* have characterized the SSA-induced photocurrent with a PIN-diode-embedded SOI ring resonator of similar geometry [2]. The on-resonance photocurrent is 25 nA at -10 V for an on-chip power of 125 μW in the bus waveguide. In contrast, the maximum photocurrent at -10 V is 590 nA in Fig. 3(a) for an on-chip power of 100 μW in the bus waveguide. We attribute this 30 \times enhancement of the photocurrent to the defect-mediated absorption.

The linear photocurrent can be calculated as [11]

$$i_{\text{ph}} = \frac{1 - \exp(-\alpha L)}{\alpha} \gamma P_1, \quad (1)$$

where P_1 is the power inside the ring after exiting the coupling section and L and α denote the perimeter and the attenuation coefficient of the ring, respectively. The carrier generation efficiency γ is determined by defect density, photon energy, and distributions of both optical mode and electrical field. The term $\gamma[1 - \exp(-\alpha L)]/\alpha$ corresponds to the slope of the curves in Fig. 3(b). Since the propagation loss of the ring is already known in Fig. 2(b), we can deduce the value of γ for different reverse biases in Fig. 3(d). In order to explore the relationship between γ and the implantation condition, we also characterize the photocurrent of a 3 mm lateral PN-junction-based Mach-Zehnder modulator (MZM) as shown in Fig. 1 from another imec run. The device is driven by a coplanar waveguide (CPW)-based traveling wave electrode that enables a >35 Gb/s modulation with a pseudorandom binary sequence (PRBS) of $2^7 - 1$ pattern length [16]. The linear relationship between the photocurrent collected from one arm of the MZM and

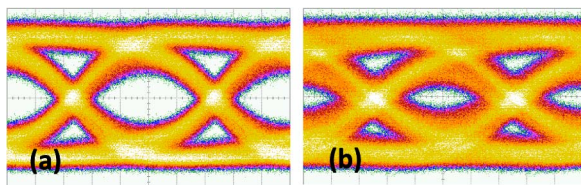


Fig. 4. (Color online) Eye diagrams of detection at (a) 25 Gbit/s and (b) 35 Gbit/s.

the optical power in this arm is shown in Fig. 3(c) for different reverse biases. Ion implantation conditions are the same as the ring modulator except that the dose is twice as high, i.e., $2 \times 10^{18}/\text{cm}^3$. Looking at only one arm of the MZM, we speculate that the defect density and the consequent carrier generation efficiency γ would scale up similarly. This is confirmed by the comparison in Fig. 3(d). Within the region where both devices are far from diode breakdown, γ of the MZM is roughly twice as high as that of the ring, e.g., $1264 \mu\text{A}/\text{mW}/\text{m}$ versus $582 \mu\text{A}/\text{mW}/\text{m}$ at -2 V . The dramatic increase of γ in the blue curve (circles) is due to the avalanche multiplication.

The overall responsivity is defined as the photocurrent divided by the optical power coupled into the device [11], i.e., the power in the bus waveguide of the ring and that entering each phase shifter of the MZM. With this definition, the responsivities are $5.9 \text{ mA}/\text{W}$ for the on-resonance ring at -10 V and $22 \text{ mA}/\text{W}$ for the 3 mm MZM at -7.1 V . The corresponding dark currents are 3 nA and $1.8 \mu\text{A}$ for the ring and the MZM, respectively. The relatively large dark current of the MZM arises from the presence of leakage current paths, which can be eliminated by adding isolation trenches.

The response speed of the photocurrent is studied by the eye diagram measurement. We choose the 3 mm MZM so as to exclude the influence of photon lifetime in the ring. In Fig. 2(a) the ring has a quality factor of 15,800 and a consequent photon-lifetime-limited 3 dB bandwidth of 12 GHz . Each arm of the MZM now can behave as a traveling wave detector. The scheme means that the input port of the CPW is terminated with a 50Ω load, while the output port is connected to an oscilloscope through an RF amplifier. A DC bias is applied on the device by a bias tee. A high bias voltage helps to enhance the responsivity as shown in Fig. 3(d). However, it should not exceed the breakdown voltage to avoid the massive diode breakdown current. Based on the above principle, the bias voltage is carefully chosen to be -7.1 V . A commercially available $40 \text{ Gb}/\text{s}$ LiNbO₃ modulator is used to encode a PRBS of $2^7 - 1$ pattern length onto a 1555 nm optical carrier at different bit rates. The optical power entering each arm of the MZM is estimated to be 8 mW . From Fig. 3(c) we speculate that the photocurrent at this power level is still dominated by the linear defect-mediated absorption. Clear open eye diagrams at 25 and 35 Gbit/s in Fig. 4 indicate that this kind of device has the potential for high-speed optical detection. The CPW here is designed for modulation rather than detection, so the performance can be improved by a dedicated RF optimization.

In conclusion, we confirm the defect-mediated subbandgap absorption in ion-implanted (boron and

phosphorus) SOI waveguides after an RTA of 1075°C . This means that the widely utilized carrier-depletion-based modulator can also be used for optical power monitoring without any additional processing. The extended functionality could have many potential applications, especially when we want to reduce the fabrication complexity. For example, carrier-depletion-based ring modulators rely on an active tuning with feedback. This usually requires a heater as well as a power monitor to control the operation wavelength. Instead of using a Ge or III-V photodiode to detect the power at the drop port of an add-drop ring, we can directly use a small section of the PN-junction-embedded ring to monitor the power inside. We expect that the responsivity can be enhanced either by using the interdigitated PN junction in [16] to enlarge the overlap between the optical mode and the carrier-depletion region or by reducing the RTA temperature to increase the crystal defect density.

The authors acknowledge the efforts of imec's 200 mm p-line for their contributions to the device fabrication. This work was supported by imec's Core Partner Program and by the EU-FP7 project SOFI (grant 248609).

References

1. J. Michel, J. Liu, and L. C. Kimerling, *Nat. Photonics* **4**, 527 (2010).
2. H. Chen, X. Luo, and A. W. Poon, *Appl. Phys. Lett.* **95**, 171111 (2009).
3. H. Chen and A. W. Poon, *Appl. Phys. Lett.* **96**, 191106 (2010).
4. T. Baehr-Jones, M. Hochberg, and A. Scherer, *Opt. Express* **16**, 1659 (2008).
5. L. D. Haret, X. Checoury, Z. Han, P. Boucaud, S. Combrié, and A. De Rossi, *Opt. Express* **18**, 23965 (2010).
6. T. Tanabe, H. Sumikura, H. Taniyama, A. Shinya, and M. Notomi, *Appl. Phys. Lett.* **96**, 101103 (2010).
7. D. F. Logan, P. Velha, M. Sorel, R. M. De La Rue, A. P. Knights, and P. E. Jessop, *IEEE Photon. Technol. Lett.* **22**, 1530 (2010).
8. M. W. Geis, S. J. Spector, M. E. Grein, R. T. Schulein, J. U. Yoon, D. M. Lennon, S. Deneault, F. Gan, F. X. Kaertner, and T. M. Lyszczarz, *IEEE Photon. Technol. Lett.* **19**, 152 (2007).
9. M. W. Geis, S. J. Spector, M. E. Grein, R. J. Schulein, J. U. Yoon, D. M. Lennon, C. M. Wynn, S. T. Palmacci, F. Gan, F. X. Käertner, and T. M. Lyszczarz, *Opt. Express* **15**, 16886 (2007).
10. M. W. Geis, S. J. Spector, M. E. Grein, J. U. Yoon, D. M. Lennon, and T. M. Lyszczarz, *Opt. Express* **17**, 5193 (2009).
11. J. K. Doylend, P. E. Jessop, and A. P. Knights, *Opt. Express* **18**, 14671 (2010).
12. Y. Liu, C. W. Cho, W. Y. Cheung, and H. K. Tsang, *IEEE Photon. Technol. Lett.* **18**, 1882 (2006).
13. J. D. B. Bradley, P. E. Jessop, and A. P. Knights, *Appl. Phys. Lett.* **86**, 241103 (2005).
14. J. K. Doylend, A. P. Knights, B. J. Luff, R. Shafiqhi, M. Asghari, and R. M. Gwilliam, *Electron. Lett.* **46**, 234 (2010).
15. M. Pantouvaki, H. Yu, P. Verheyen, G. Lepage, W. Bogaerts, M. Moelants, J. Wouters, D. Radisic, P. Absil, and J. Van Campenhout, in *Proceedings of IEEE Conference on Optical Interconnects* (IEEE, 2012), pp. 44–45.
16. H. Yu, M. Pantouvaki, J. Van Campenhout, D. Korn, K. Komorowska, P. Dumon, Y. Li, P. Verheyen, P. Absil, L. Alloatti, D. Hillerkuss, J. Leuthold, R. Baets, and W. Bogaerts, *Opt. Express* **20**, 12926 (2012).